Article

Not peer-reviewed version

Influence of Ni Doping on Oxygen Vacancy-Induced Changes in Structural and Chemical Properties of CeO2 Nanorods

Yuanzheng Zhu , Weixia Wang , Gejunxiang Chen , Huyi Li , Yuedie Zhang , Chang Liu , Hao Wang ,
Ping Cheng * , Chunguang Chen * , Gimyeong Seong *

Posted Date: 26 March 2024

doi: 10.20944/preprints202403.1599.v1

Keywords: cerium dioxide; Ni doping; oxygen vacancies; hydrothermal synthesis

Preprints.org (www.preprints.org) | NOT PEER-REVIEWED | Posted: 26 March 2024 doi:10.20944/preprints202403.1599.v1

Article

Influence of Ni Doping on Oxygen Vacancy-Induced Changes in Structural and Chemical Properties of CeO_2 Nanorods

Yuanzheng Zhu [1], Weixia Wang [1], Gejunxiang Chen [1], Huyi Li [1], Yuedie Zhang [1], Chang Liu [1], Hao Wang [1], Ping Cheng [1,*], Chunguang Chen [1,*] and Gimyeong Seong [2,*]

[1] School of Materials and Chemistry, University of Shanghai for Science and Technology, Shanghai 200093, China; zyz@usst.edu.cn (Y.Z.); 232162987@st.usst.edu.cn (W.W.); 2135050408@st.usst.edu.cn (G.C.); 1158233395@qq.com (H.L.); 213352421@st.usst.edu.cn (Y.Z.); 223353262@st.usst.edu.cn (C.L.); 2026010221@st.usst.edu.cn (H.W.)

[2] Department of Environmental & Energy, Engineering, The University of Suwon, 17, Wauan-gil, Bongdam-eup, Hwaseong-si, Gyeonggi-do 18323, Republic of Korea

* Correspondence: chengp@usst.edu.cn (P.C.); cgchen19@usst.edu.cn (C.C.); soppua4@suwon.ac.kr (G.S.)

Abstract: In recent years, cerium dioxide (CeO_2) has attracted considerable attention owing to its remarkable performance in various applications, including photocatalysis, fuel cells, and catalysis. This study explores the effect of nickel (Ni) doping on the structural, thermal, and chemical properties of CeO_2 nanorods, particularly focusing on oxygen vacancy-related phenomena. Utilizing X-ray powder diffraction (XRD), alterations in crystal structure and peak shifts were observed, indicating successful Ni doping and the formation of Ni_2O_3 at higher doping levels, likely due to non-equilibrium reactions. Thermal gravimetric analysis (TGA) revealed changes in oxygen release mechanisms, with increasing Ni doping resulting in the release of lattice oxygen at lower temperatures. Raman spectroscopy corroborated these findings by identifying characteristic peaks associated with oxygen vacancies, facilitating the assessment of Ni doping levels. Overall, this study underscores the substantial impact of Ni doping on CeO_2 nanorods, shedding light on tailored catalytic applications through modulation of oxygen vacancies while preserving the nanorod morphology.

Keywords: cerium dioxide; Ni doping; oxygen vacancies; hydrothermal synthesis

1. Introduction

In recent years, cerium dioxide (CeO_2), as a typical rare earth metal oxide, has received widespread attention due to its excellent performance in photocatalysis [1–3], fuel cells [4–7], sensors [8–11], CO oxidation [12–16], water gas shift reaction [17–20], and other fields [21–23]. This is mainly attributed to its two important characteristics. Firstly, in the CeO_2 lattice, rapid conversion of two valence states (Ce^{4+}/Ce^{3+}) is achieved through the formation/loss of oxygen vacancies, thus CeO_2 has excellent redox ability [24]. Secondly, CeO_2 has a cubic fluorite structure containing many oxygen vacancies, which are beneficial for improving oxygen mobility [25,26].

CeO_2 is an n-type semiconductor material with oxygen vacancies sites. The Kroger- Vink formula is expressed as $2CeO_2=2Ce'_{Ce}+V^{\cdot\cdot}_{O}+3O_O^{x}+1/2O_2\uparrow$, where Ce'_{Ce} represents the presence of one-unit negative charge at the Ce^{4+} position, $V^{\cdot\cdot}_{O}$ represents an oxygen vacancy with a two-units positive charge, and O_O^{x} represents the oxygen atom on the CeO_2 lattice site. The presence of oxygen vacancies generates Ce^{3+}, therefore CeO_2 has a high lattice ion mobility and excellent oxygen storage and release ability and is used as a catalyst in various fields [27].

CeO_2 nanocrystals typically expose low index crystal planes (111), (110), and (100) [28]. Theoretical calculations indicate that the (110) plane has the lowest vacancy formation energy of 1.99

eV, the (100) plane has a vacancy formation energy of 2.27 eV, and the most stable (111) plane has a maximum vacancy formation energy of 2.60 eV. Consequently, the order of the formation energy of oxygen vacancies on different crystal planes of CeO_2 is: (110)<(100)<(111) [29]. Therefore, the formation of oxygen vacancies on the CeO_2 (110) crystal plane is easier. CeO_2 has different exposed crystal planes based on its morphology. Polyhedral CeO_2 mainly exposes (111) crystal planes, while cubic CeO_2 mainly exposes (100) crystal planes and rod-shaped CeO_2 mainly simultaneously exposes (110) and (100) crystal planes [28]. It is possible to regulate the morphology of CeO_2 to alter oxygen vacancies. Yuan investigated that the effect of CeO_2 morphology on the catalytic activity of nitrobenzene hydrogen transfer reduction reaction. Oxygen vacancies and basic sites can selectively activate ethanol molecules to reduce nitro groups. The catalytic activity is sorted in the order: CeO_2 nanorods, CeO_2 nanopolyhedrons, and CeO_2 nanocubes [30].

Doping different metals, such as precious metals, transition metals, alkali metals, and rare earth metals, into the CeO_2 lattice can improve its catalytic activity and stability [31,32]. Through metal doping, lattice distortion can be induced, resulting in abundant oxygen vacancies and Ce^{3+}, which are widely used in catalysis [33]. Transition metal catalysts have received considerable attention due to their low cost and excellent activity. Researchers have found that the substitution of Ce^{4+} with transition metals can significantly alter the geometric and electronic structures of CeO_2 systems, leading to the reappearance of enriched electronic regions in CeO_2 and weakening of Ce-O or M-O bonds [34,35]. The results indicate that the atomic radius has a significant impact on the structure of doped CeO_2, and radii larger or smaller than those of Ce^{4+} ions usually produce significant geometric distortions. La doped CeO_2 nanorod shows significantly higher H_2 production compared to CeO_2 in photocatalytic reaction [36]. We selected the fourth period transition metal element Ni, which has the advantage of low cost, as the doping element to investigate its effect on oxygen vacancies in CeO_2.

In this article, we control the concentration of oxygen vacancies in CeO_2 by combining morphology control and metal ion doping, thereby affecting its catalytic activity. This study prepared a series of Ni-doped CeO_2 nanorods using the hydrothermal method. In addition, the structural, thermal stability, changes in oxygen vacancy concentration between CeO_2 and the doped CeO_2 nanorods were thoroughly analyzed using a combination of X-ray power diffusion (XRD), transmission electron microscopy (TEM), thermogravimetry analysis (TGA), and Raman spectroscopy.

2. Materials and Methods

2.1. Reagents

Cerium(III) nitrate hexahydrate ($Ce(NO_3)_3{\cdot}6H_2O$, 99.9%, AR) was purchased from Shanghai Civi Chemical Technology Co., Ltd. (Shanghai, China). Nickel nitrate hexahydrate ($Ni(NO_3)_3{\cdot}6H_2O$, 99%, AR) was obtained from J&K Scientific (Beijing, China), and sodium hydroxide (NaOH, 99%, AR) was sourced from Shanghai Titan Scientific Co., Ltd. (Shanghai, China). Ultrapure water was produced using a laboratory water purification system (Hetai, China). All chemicals were used as received without further purification.

2.2. Hydrothermal Synthesis of Ni-Doped CeO_2 Nanorods

Ni-doped CeO_2 nanorods with various Ni^{2+} contents (0, 1, 5, 15 at%) were synthesized using the modified hydrothermal method, as described in Mai's work [28]. $Ce(NO_3)_3{\cdot}6H_2O$ and $Ni(NO_3)_3{\cdot}6H_2O$ with different molar ratios were dissolved in 5 mL deionized water. Meanwhile, 12.6 g of NaOH was dissolved in 30 mL of deionized water. Afterward, the two solutions were uniformly mixed and stirred at room temperature for 30 min. The resulting mixture was transferred to a 50 mL autoclave, which was then sealed and maintained at 373 K for 24 h. Subsequently, the autoclave was allowed to cool down to room temperature, and the obtained product was centrifuged and washed with deionized water and ethanol three times. The product was then dried overnight at 333 K and subsequently calcined at 673 K for 2 h under an air atmosphere.

doi:10.20944/preprints202403.1599.v1

2.3. Characterization

The X-ray powder Diffraction (XRD) patterns were recorded using a Rigaku diffractometer with Cu Kα radiation (λ=1.5418 nm). The X-rays were operated at 40 kV and 40 mA. Patterns were collected in the 2θ range from 20° to 80°, with a scanning step of 0.02 and a scanning speed of 2.5°/min. The morphology and microstructure of the samples were characterized using a HT7800 transmission electron microscope (TEM) operating at 200 kV. Thermal gravimetric analysis (TGA-50, Shimadzu Corp., Japan) was employed to measure oxygen release with temperature increase. The temperature was raised from room temperature to 800 ℃ at a rate of 10 ℃/min under a nitrogen atmosphere (gas flow rate: 24 mL/min). Raman spectroscopy was utilized to measure the presence of surface Ce^{3+} or oxygen vacancies. This analysis was performed at the Shanghai branch of the Beijing High Voltage Science Research Center (Gaoke) using the Renishaw inVia micro Raman spectrometer from the UK. The experiment employed a 532 nm laser light source with a power of 50 mW, 1800 gr/mm grating, and a 50 times Leica long focal length lens. The required Raman spectrum for this experiment covers a scanning range of 50–1200 cm^{-1}, with a scanning time of 10 seconds, 10 scanning times, and a resolution of 3 cm^{-1}.

3. Results and Discussion

The phase structure of the products was characterized by X-ray powder diffraction (XRD), as shown in Figure 1. The characteristic diffraction peaks of pure CeO_2 samples appear at 28.5°, 33.1°, 47.5°, 56.3°, 59.1°, 69.4°, 76.7°, and 79.1°, corresponding to the cubic fluorite crystal planes of CeO_2 for (111), (200), (220), (311), (222), (400), (331), and (420), respectively. As the Ni doping amount increases, the width of the diffraction peaks also increases, indicating a decrease in crystallite size with increasing Ni doping amount (Table 1.). Additionally, upon comparison with the (111) peak of pure CeO_2, the peaks of the doped samples are observed to shift to lower angles. This phenomenon occurs due to the replacement of cerium sites in the cerium oxide lattice by Ni^{2+}, with a radius of 0.63 Å, resulting in the observed shift of the cerium oxide peaks [37,38]. This shift indicates the successful doping of metallic nickel into the cerium oxide lattice. According to the Bragg equation, $2d\sin\theta = n\lambda$, after doping with nickel metal, the decrease in θ value leads to a slight increase in the interplanar spacing of the crystal cell, causing slight lattice expansion [39]. However, this does not significantly affect the crystal cell structure of ceria itself. When the doping amount is increased to 15%, a new diffraction peak appears near 38°, corresponding to the standard diffraction peak of Ni_2O_3. This indicates the generation of Ni_2O_3 from some undoped metal Ni. However, no diffraction peak of Ni_2O_3 is observed at doping levels of 1% and 5%, suggesting that nickel can be completely doped into CeO_2 at low doping levels.

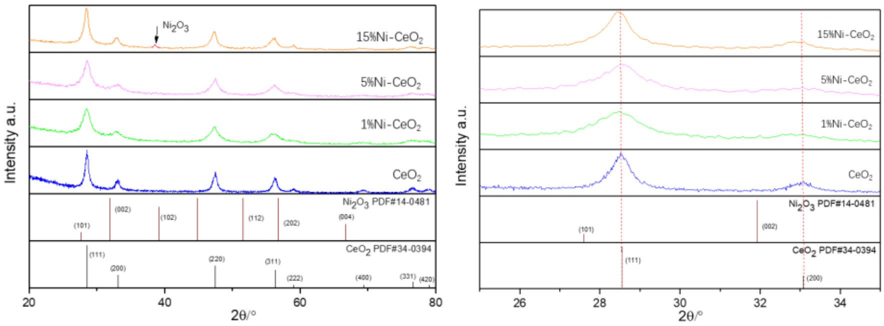

Figure 1. XRD spectra of CeO_2 and Ni-doped CeO_2.

Table 1. Lattice constant and crystallite size of the samples.

	CeO_2	1%Ni-CeO_2	5% Ni-CeO_2	15% Ni-CeO_2
Lattice constant (Å)	5.4110	5.4064	5.3982	5.4230
Crystallite size (nm)	128	65	60	92

Figure 2(a–d) presents TEM images of CeO_2 and Ni-doped CeO_2. It is evident that rod-shaped CeO_2 nanomaterials have been successfully synthesized. As depicted in Figure 2(b), even with a 1% doping amount, the rod-shaped morphology of CeO_2 nanomaterials remains unchanged. With a doping amount of 5% (Figure 2(c)), the rod-shaped structure becomes wider. In Figure 2(d), with a doping amount of 15%, although the structure remains rod-shaped, the length of the rods significantly decreases while the width increases.

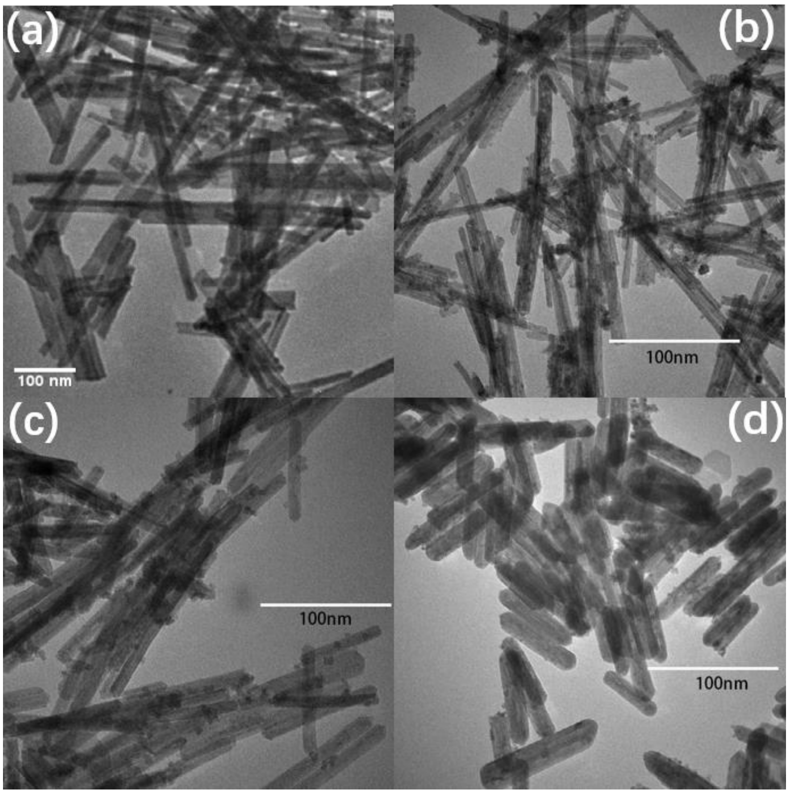

Figure 2. TEM images of CeO_2 and Ni-doped CeO_2: (a) CeO_2; (b)1% Ni-CeO_2; (c)5% Ni-CeO_2; (d)15% Ni-CeO_2.

Figure 3 shows the thermogravimetric analysis of undoped CeO_2 and Ni-doped CeO_2 nanorods. Up to about 150 °C, the weight loss due to the loss of surface moisture can be ignored. Therefore, the weight loss above 150 °C can be attributed to the loss of surface or lattice oxygen. It can be observed that the pattern of weight loss changes around 320 °C, indicating different energy release mechanisms between surface and lattice oxygen [40,41]. By analyzing the weight loss in each temperature range, the weight loss due to surface oxygen release was approximately 2 wt% for pure CeO_2, 5 wt% for 1% Ni-CeO_2, 4 wt% for 5% Ni-CeO_2, and 3 wt% for 15% Ni-CeO_2. On the other hand, the weight loss due to lattice oxygen release was approximately 1 wt% for pure CeO_2, 5 wt% for 1% Ni-CeO_2, 2 wt% for 5% Ni-CeO_2, and 1 wt% for 15% Ni-CeO_2. The weight loss rate after Ni doping was higher than that without doping, except for 1% Ni-CeO_2, and generally decreased with increasing doping level (Table 2.). This may be attributed to the non-equilibrium reactions leading to the formation of NiO_x when Ni is added at high concentrations [42]. Furthermore, as the doping effect increases, the activation of surface oxygen also increases, leading to a greater impact on weight loss at lower temperatures. In other words, in the temperature range below 800 °C, the influence of surface oxygen release becomes more significant with increasing doping. Calculating the ratio of surface oxygen to lattice oxygen, it increased to 1 for 1% Ni-CeO_2, 2 for 5% Ni-CeO_2, and 3 for 15% Ni-CeO_2.

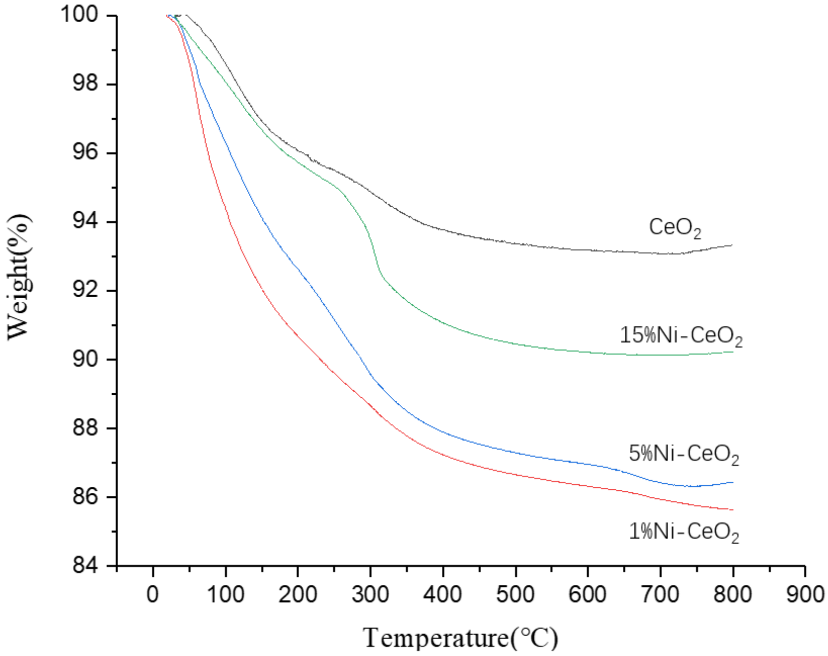

Figure 3. The TG curve of CeO_2 and Ni-doped CeO_2.

Table 2. The ratio of surface oxygen/lattice oxygen of samples.

	CeO_2	**1%Ni-CeO_2**	5% **Ni-CeO_2**	15% **Ni-CeO_2**
Surface oxygen	2wt%	5wt%	4wt%	3wt%
Lattice oxygen	1wt%	5wt%	2wt%	1wt%
Total oxygen	3wt%	10wt%	6wt%	4wt%

Figure 4, the Raman spectra provide the following insights: both undoped and Ni-doped CeO_2 samples exhibit characteristic peaks around 462 cm^{-1}, originating from the F_2g vibration of CeO_2 due to the symmetric arrangement of oxygen atoms in the CeO_2 lattice [43]. Additionally, a weak absorption peak is observed near 595 cm^{-1}, corresponding to Frenkel-type oxygen vacancies [44]. Notably, the characteristic peak of undoped CeO_2 at 462 cm^{-1} appears strongest among the four images. As the doping level of Ni increases, the intensity of absorption peaks at this location gradually diminishes due to the substitutional reaction $Ce^{4+} + Ni^{2+} \leftrightarrow Ni^{3+} + Ce^{3+}$, leading to the generation of oxygen vacancies and thus symmetry degradation [45,46].

To gauge the relative concentration of surface oxygen vacancies in the samples, the intensity of the absorption peak at 595 cm^{-1} (A_{595}) was compared to that at 462 cm^{-1} (A_{462}) [47]. A higher ratio indicates a greater presence of oxygen vacancies on the sample surface [48,49]. Specific ratios are provided in Table 3. As evident from these findings, increasing Ni doping correlates with a rise in the concentration of oxygen vacancies on the surface of cerium dioxide, peaking at a 5% doping level.

However, at a 15% doping level, the peak intensity slightly decreases, attributed to incomplete Ni doping and the formation of Ni_2O_3, consistent with previous discussions.

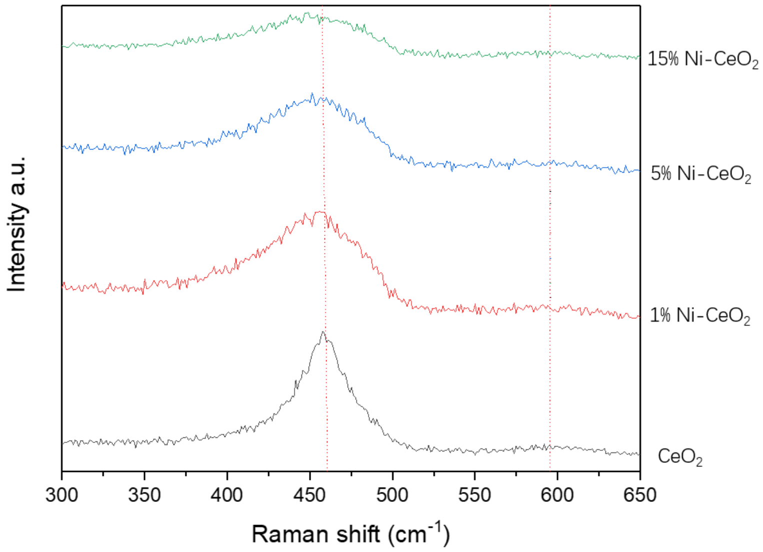

Figure 4. Raman spectra of CeO_2 and Ni-doped CeO_2.

Table 3. The ratio of A_{595}/A_{462} in Raman spectra.

	CeO_2	**1%Ni-CeO_2**	5%Ni-**CeO_2**	15%Ni-**CeO_2**
A_{595}/A_{462}	9.79%	23.9%	30.5%	26.7%

4. Conclusions

Summarizing the research findings, it can be concluded that doping Ni into CeO_2 nanorods significantly impacts their structural, thermal, and chemical properties. XRD analysis revealed changes in crystal structure and peak shifts, indicating successful Ni doping and the formation of Ni_2O_3 at high doping levels due to non-equilibrium reactions. TGA results demonstrated variations in oxygen release mechanisms, with increasing Ni doping leading to the emission of some lattice oxygen at lower temperatures, as confirmed by changes in weight ratio across temperature ranges. Additionally, the presence of characteristic Raman peaks associated with oxygen vacancies allowed for assessing the extent of Ni doping based on peak intensity changes. Therefore, through this study, successful adjustment of properties for catalytic applications was achieved by controlling the Ni doping level while maintaining the CeO_2 nanorod type.

Author Contributions: Conceptualization, Y.Z.; methodology, Y.Z.; investigation, W.W., H.L., Y.Z.(Yuedie Zhang), C.L.; data curation, H.L., G.C., H.W.; writing—original draft preparation, Y.Z.; writing—review and editing, G.S.; supervision, P.C., C.C., G.S.. All authors have read and agreed to the published version of the manuscript.

Funding: This research was funded by the research grant of The University of Suwon in 2023.

Data Availability Statement: The data presented in this study are available within this article.

Acknowledgments: This research was supported by the "College Student Innovation Training Program" of University of Shanghai for Science and Technology (XJ2023484).

Conflicts of Interest: The authors declare no conflict of interest.

References

1. Yang, J.; Xie, N.; Zhang, J.; Fan, W.; Huang, Y.; Tong, Y. Defect Engineering Enhances the Charge Separation of CeO_2 Nanorods toward Photocatalytic Methyl Blue Oxidation. *Nanomaterials* **2020**, *10*, 2307, doi:10.3390/nano10112307.
2. Murray, S.; Wei, W.; Hart, R.; Fan, J.; Chen, W.; Lu, P. Solar Degradation of Toxic Colorants in Polluted Water by Thermally Tuned Ceria Nanocrystal-Based Nanofibers. *ACS Appl. Nano Mater.* **2020**, *3*, 11194–11202, doi:10.1021/acsanm.0c02324.
3. Yu, D.; Jia, Y.; Yang, Z.; Zhang, H.; Zhao, J.; Zhao, Y.; Weng, B.; Dai, W.; Li, Z.; Wang, P.; et al. Solar Photocatalytic Oxidation of Methane to Methanol with Water over RuO_x/ZnO/CeO_2 Nanorods. *ACS Sustain. Chem. Eng.* **2022**, *10*, 16–22, doi:10.1021/acssuschemeng.1c07162.
4. Chen, T.; Zheng, G.; Liu, K.; Zhang, G.; Huang, Z.; Liu, M.; Zhou, J.; Wang, S. Application of CuNi–CeO_2 Fuel Electrode in Oxygen Electrode Supported Reversible Solid Oxide Cell. *Int. J. Hydrog. Energy* **2023**, *48*, 9565–9573, doi:10.1016/j.ijhydene.2022.11.236.
5. Zhao, M.; Geng, S.; Chen, G.; Wang, F. Efficient FeCoNi/CeO_2 Coatings for Solid Oxide Fuel Cell Steel Interconnect Applications. *Int. J. Hydrog. Energy* **2024**, *50*, 1087–1094, doi:10.1016/j.ijhydene.2023.10.030.
6. Li, J.; Xie, J.; Li, D.; Yu, L.; Xu, C.; Yan, S.; Lu, Y. An Interface Heterostructure of NiO and CeO_2 for Using Electrolytes of Low-Temperature Solid Oxide Fuel Cells. *Nanomaterials* **2021**, *11*, 2004, doi:10.3390/nano11082004.
7. Zhang, Y.; Zhu, D.; Jia, X.; Liu, J.; Li, X.; Ouyang, Y.; Li, Z.; Gao, X.; Zhu, C. Novel n–i CeO_2 /a-Al_2O_3 Heterostructure Electrolyte Derived from the Insulator a-Al_2O_3 for Fuel Cells. *ACS Appl. Mater. Interfaces* **2023**, *15*, 2419–2428, doi:10.1021/acsami.2c18240.
8. Ema, T.; Choi, P.G.; Takami, S.; Masuda, Y. Facet-Controlled Synthesis of CeO_2 Nanoparticles for High-Performance CeO_2 Nanoparticle/SnO_2 Nanosheet Hybrid Gas Sensors. *ACS Appl. Mater. Interfaces* **2022**, *14*, 56998–57007, doi:10.1021/acsami.2c17444.
9. Hu, Q.; Huang, B.; Li, Y.; Zhang, S.; Zhang, Y.; Hua, X.; Liu, G.; Li, B.; Zhou, J.; Xie, E.; et al. Methanol Gas Detection of Electrospun CeO2 Nanofibers by Regulating Ce3+/ Ce4+ Mole Ratio via Pd Doping. *Sens. Actuators B Chem.* **2020**, *307*, 127638, doi:10.1016/j.snb.2019.127638.
10. Hu, Q.; Jiang, H.; Zhang, W.; Wang, X.; Wang, X.; Zhang, Z. Unveiling the Synergistic Effects of Hydrogen Annealing on CeO_2 Nanofibers for Highly Sensitive Acetone Gas Detection: Role of Ce3+ Ions and Oxygen Vacancies. *Appl. Surf. Sci.* **2023**, *640*, 158411, doi:10.1016/j.apsusc.2023.158411.
11. Yuan, K.; Wang, C.-Y.; Zhu, L.-Y.; Cao, Q.; Yang, J.-H.; Li, X.-X.; Huang, W.; Wang, Y.-Y.; Lu, H.-L.; Zhang, D.W. Fabrication of a Micro-Electromechanical System-Based Acetone Gas Sensor Using CeO_2 Nanodot-Decorated WO_3 Nanowires. *ACS Appl. Mater. Interfaces* **2020**, *12*, 14095–14104, doi:10.1021/acsami.9b18863.
12. Basina, G.; Polychronopoulou, K.; Zedan, A.F.; Dimos, K.; Katsiotis, M.S.; Fotopoulos, A.P.; Ismail, I.; Tzitzios, V. Ultrasmall Metal-Doped CeO_2 Nanoparticles for Low-Temperature CO Oxidation. *ACS Appl. Nano Mater.* **2020**, *3*, 10805–10813, doi:10.1021/acsanm.0c02090.
13. Ahasan, M.R.; Wang, R. CeO2 Nanorods Supported CuOx-RuOx Bimetallic Catalysts for Low Temperature CO Oxidation. *J. Colloid Interface Sci.* **2024**, *654*, 1378–1392, doi:10.1016/j.jcis.2023.10.113.
14. Fan, J.; Hu, S.; Li, C.; Wang, Y.; Chen, G. Effect of Loading Method on Catalytic Performance of Pt/CeO_2 System for CO Oxidation. *Mol. Catal.* **2024**, *558*, 114013, doi:10.1016/j.mcat.2024.114013.
15. Kim, H.Y.; Lee, H.M.; Henkelman, G. CO Oxidation Mechanism on CeO_2 -Supported Au Nanoparticles. *J. Am. Chem. Soc.* **2012**, *134*, 1560–1570, doi:10.1021/ja207510v.

16. Zhou, Z.; Zhang, J.; Liu, Y. Promoted Low-Temperature CO Oxidation Activity of CeO_2 by Cu Doping: The Important Role of Oxygen Vacancies. *Fuel* **2024**, *359*, 130434, doi:10.1016/j.fuel.2023.130434.
17. Reina, T.R.; Gonzalez-Castaño, M.; Lopez-Flores, V.; Martínez T, L.M.; Zitolo, A.; Ivanova, S.; Xu, W.; Centeno, M.A.; Rodriguez, J.A.; Odriozola, J.A. Au and Pt Remain Unoxidized on a CeO_2 -Based Catalyst during the Water–Gas Shift Reaction. *J. Am. Chem. Soc.* **2022**, *144*, 446–453, doi:10.1021/jacs.1c10481.
18. Yu, J.; Qin, X.; Yang, Y.; Lv, M.; Yin, P.; Wang, L.; Ren, Z.; Song, B.; Li, Q.; Zheng, L.; et al. Highly Stable Pt/CeO_2 Catalyst with Embedding Structure toward Water–Gas Shift Reaction. *J. Am. Chem. Soc.* **2024**, *146*, 1071–1080, doi:10.1021/jacs.3c12061.
19. Shen, X.; Li, Z.; Xu, J.; Li, W.; Tao, Y.; Ran, J.; Yang, Z.; Sun, K.; Yao, S.; Wu, Z.; et al. Upgrading the Low Temperature Water Gas Shift Reaction by Integrating Plasma with a CuOx/CeO_2 Catalyst. *J. Catal.* **2023**, *421*, 324–331, doi:10.1016/j.jcat.2023.03.033.
20. Zhang, K.; Guo, Q.; Wang, Y.; Cao, P.; Zhang, J.; Heggen, M.; Mayer, J.; Dunin-Borkowski, R.E.; Wang, F. Ethylene Carbonylation to 3-Pentanone with In Situ Hydrogen via a Water–Gas Shift Reaction on Rh/CeO_2. *ACS Catal.* **2023**, *13*, 3164–3169, doi:10.1021/acscatal.2c06123.
21. Yu, Y.; He, J.; Wang, T.; Qiu, X.; Chen, K.; Wu, Q.; Shi, D.; Zhang, Y.; Li, H. One-Step Production of Pt–CeO_2/N-CNTs Electrocatalysts with High Catalytic Performance toward Methanol Oxidation. *Int. J. Hydrog. Energy* **2023**, *48*, 29565–29582, doi:10.1016/j.ijhydene.2023.04.137.
22. Jiang, F.; Wang, S.; Liu, B.; Liu, J.; Wang, L.; Xiao, Y.; Xu, Y.; Liu, X. Insights into the Influence of CeO_2 Crystal Facet on CO_2 Hydrogenation to Methanol over Pd/CeO_2 Catalysts. *ACS Catal.* **2020**, *10*, 11493–11509, doi:10.1021/acscatal.0c03324.
23. Guo, Y.; Qin, Y.; Liu, H.; Wang, H.; Han, J.; Zhu, X.; Ge, Q. CeO_2 Facet-Dependent Surface Reactive Intermediates and Activity during Ketonization of Propionic Acid. *ACS Catal.* **2022**, *12*, 2998–3012, doi:10.1021/acscatal.1c05994.
24. Reed, K.; Cormack, A.; Kulkarni, A.; Mayton, M.; Sayle, D.; Klaessig, F.; Stadler, B. Exploring the Properties and Applications of Nanoceria: Is There Still Plenty of Room at the Bottom? *Env. Sci Nano* **2014**, *1*, 390–405, doi:10.1039/C4EN00079J.
25. Chauhan, S.; Richards, G.J.; Mori, T.; Yan, P.; Hill, J.P.; Ariga, K.; Zou, J.; Drennan, J. Fabrication of a Nano-Structured Pt-Loaded Cerium Oxide Nanowire and Its Anode Performance in the Methanol Electro-Oxidation Reaction. *J. Mater. Chem. A* **2013**, *1*, 6262, doi:10.1039/c3ta10652g.
26. Li, G.; Lu, F.; Wei, X.; Song, X.; Sun, Z.; Yang, Z.; Yang, S. Nanoporous Ag–CeO_2 Ribbons Prepared by Chemical Dealloying and Their Electrocatalytic Properties. *J. Mater. Chem. A* **2013**, *1*, 4974, doi:10.1039/c3ta01506h.
27. Wu, K.; Sun, L.; Yan, C. Recent Progress in Well-Controlled Synthesis of Ceria-Based Nanocatalysts towards Enhanced Catalytic Performance. *Adv. Energy Mater.* **2016**, *6*, 1600501, doi:10.1002/aenm.201600501.
28. Mai, H.-X.; Sun, L.-D.; Zhang, Y.-W.; Si, R.; Feng, W.; Zhang, H.-P.; Liu, H.-C.; Yan, C.-H. Shape-Selective Synthesis and Oxygen Storage Behavior of Ceria Nanopolyhedra, Nanorods, and Nanocubes. *J. Phys. Chem. B* **2005**, *109*, 24380–24385, doi:10.1021/jp055584b.
29. Nolan, M.; Fearon, J.; Watson, G. Oxygen Vacancy Formation and Migration in Ceria. *Solid State Ion.* **2006**, *177*, 3069–3074, doi:10.1016/j.ssi.2006.07.045.
30. Yuan, Z.; Huang, L.; Liu, Y.; Sun, Y.; Wang, G.; Li, X.; Lercher, J.A.; Zhang, Z. Synergy of Oxygen Vacancies and Base Sites for Transfer Hydrogenation of Nitroarenes on Ceria Nanorods. *Angew. Chem.* **2024**, *136*, e202317339, doi:10.1002/ange.202317339.

31. Abdulwahab, K.O.; Khan, M.M.; Jennings, J.R. Doped Ceria Nanomaterials: Preparation, Properties, and Uses. *ACS Omega* **2023**, *8*, 30802–30823, doi:10.1021/acsomega.3c01199.
32. Hajjiah, A.; Samir, E.; Shehata, N.; Salah, M. Lanthanide-Doped Ceria Nanoparticles as Backside Coaters to Improve Silicon Solar Cell Efficiency. *Nanomaterials* **2018**, *8*, 357, doi:10.3390/nano8060357.
33. Thormann, J.; Maier, L.; Pfeifer, P.; Kunz, U.; Deutschmann, O.; Schubert, K. Steam Reforming of Hexadecane over a Rh/CeO_2 Catalyst in Microchannels: Experimental and Numerical Investigation. *Int. J. Hydrog. Energy* **2009**, *34*, 5108–5120, doi:10.1016/j.ijhydene.2009.04.031.
34. Yildirim, H.; Pachter, R. Extrinsic Dopant Effects on Oxygen Vacancy Formation Energies in ZrO_2 with Implication for Memristive Device Performance. *ACS Appl. Electron. Mater.* **2019**, *1*, 467–477, doi:10.1021/acsaelm.8b00090.
35. Sen, S.; Edwards, T.; Kim, S.K.; Kim, S. Investigation of the Potential Energy Landscape for Vacancy Dynamics in Sc-Doped CeO_2. *Chem. Mater.* **2014**, *26*, 1918–1924, doi:10.1021/cm4041852.
36. Nabi, G.; Ali, W.; Majid, A.; Alharbi, T.; Saeed, S.; Albedah, M.A. Controlled Growth of Bi-Functional La Doped CeO_2 Nanorods for Photocatalytic H_2 Production and Supercapacitor Applications. *Int. J. Hydrog. Energy* **2022**, *47*, 15480–15490, doi:10.1016/j.ijhydene.2022.02.184.
37. Xiao, M.; Han, D.; Yang, X.; Tsona Tchinda, N.; Du, L.; Guo, Y.; Wei, Y.; Yu, X.; Ge, M. Ni-Doping-Induced Oxygen Vacancy in Pt-CeO_2 Catalyst for Toluene Oxidation: Enhanced Catalytic Activity, Water-Resistance, and SO_2-Tolerance. *Appl. Catal. B Environ.* **2023**, *323*, 122173, doi:10.1016/j.apcatb.2022.122173.
38. Yang, Z.; Zheng, D.; Yue, X.; Wang, K.; Hou, Y.; Dai, W.; Fu, X. The Synergy of Ni Doping and Oxygen Vacancies over CeO_2 in Visible Light-Assisted Thermal Catalytic Methanation Reaction. *Appl. Surf. Sci.* **2023**, *615*, 156311, doi:10.1016/j.apsusc.2022.156311.
39. Liu, Z.; Ma, H.; Sorrell, C.C.; Koshy, P.; Wang, B.; Hart, J.N. Enhancement of Light Absorption and Oxygen Vacancy Formation in CeO_2 by Transition Metal Doping: A DFT Study. *Appl. Catal. Gen.* **2024**, *670*, 119544, doi:10.1016/j.apcata.2023.119544.
40. Lee, J.; Ryou, Y.; Chan, X.; Kim, T.J.; Kim, D.H. How Pt Interacts with CeO_2 under the Reducing and Oxidizing Environments at Elevated Temperature: The Origin of Improved Thermal Stability of Pt/CeO_2 Compared to CeO_2. *J. Phys. Chem. C* **2016**, *120*, 25870–25879, doi:10.1021/acs.jpcc.6b08656.
41. D'Angelo, A.M.; Wu, Z.; Overbury, S.H.; Chaffee, A.L. Cu-Enhanced Surface Defects and Lattice Mobility of Pr-CeO_2 Mixed Oxides. *J. Phys. Chem. C* **2016**, *120*, 27996–28008, doi:10.1021/acs.jpcc.6b08947.
42. Zhu, Y.; Seong, G.; Noguchi, T.; Yoko, A.; Tomai, T.; Takami, S.; Adschiri, T. Highly Cr-Substituted CeO_2 Nanoparticles Synthesized Using a Non-Equilibrium Supercritical Hydrothermal Process: High Oxygen Storage Capacity Materials Designed for a Low-Temperature Bitumen Upgrading Process. *ACS Appl. Energy Mater.* **2020**, *3*, 4305–4319, doi:10.1021/acsaem.0c00026.
43. Shyu, J.Z.; Weber, W.H.; Gandhi, H.S. Surface Characterization of Alumina-Supported Ceria. *J. Phys. Chem.* **1988**, *92*, 4964–4970, doi:10.1021/j100328a029.
44. Popović, Z.V.; Dohčević-Mitrović, Z.; Konstantinović, M.J.; Šćepanović, M. Raman Scattering Characterization of Nanopowders and Nanowires (Rods). *J. Raman Spectrosc.* **2007**, *38*, 750–755, doi:10.1002/jrs.1696.
45. Du, X.; Dai, Q.; Wei, Q.; Huang, Y. Nanosheets-Assembled Ni (Co) Doped CeO_2 Microspheres toward NO + CO Reaction. *Appl. Catal. Gen.* **2020**, *602*, 117728, doi:10.1016/j.apcata.2020.117728.
46. Tiwari, S.; Khatun, N.; Patra, N.; Yadav, A.K.; Bhattacharya, D.; Jha, S.N.; Tseng, C.M.; Liu, S.W.; Biring, S.; Sen, S. Role of Oxygen Vacancies in Co/Ni Substituted CeO_2: A Comparative Study. *Ceram. Int.* **2019**, *45*, 3823–3832, doi:10.1016/j.ceramint.2018.11.053.

47. Li, L.; Chen, F.; Lu, J.-Q.; Luo, M.-F. Study of Defect Sites in $Ce_{1-x}M_xO_{2-\delta}$ ($x = 0.2$) Solid Solutions Using Raman Spectroscopy. *J. Phys. Chem. A* **2011**, *115*, 7972–7977, doi:10.1021/jp203921m.
48. Zhao, P.; Feng, N.; Tan, B.; Huo, Z.; Liu, G.; Wan, H.; Guan, G. Exposed Crystal Facet Tuning of CeO_2 for Boosting Catalytic Soot Combustion: The Effect of La Dopant. *J. Environ. Chem. Eng.* **2022**, *10*, 108503, doi:10.1016/j.jece.2022.108503.
49. Cao, Y.; Zhao, L.; Gutmann, T.; Xu, Y.; Dong, L.; Buntkowsky, G.; Gao, F. Getting Insights into the Influence of Crystal Plane Effect of Shaped Ceria on Its Catalytic Performances. *J. Phys. Chem. C* **2018**, *122*, 20402–20409, doi:10.1021/acs.jpcc.8b06138.